21 Spherical and Chromatic Aberration Correction for Atomic-Resolution Liquid Cell Electron Microscopy

Rafal E. Dunin-Borkowski and Lothar Houben

21.1 Introduction

Compared with carrying out liquid cell experiments in an uncorrected electron microscope, spherical aberration correction in the TEM and STEM can be used to improve spatial resolution, as discussed in Chapter 8. Spherical aberration correction also improves the depth of field, allows the effects of image delocalization to be minimized, provides better precision in measurement of the positions of features of interest in the sample, and facilitates the quantitative comparison of experimental images with computer simulations in terms of absolute intensities rather than arbitrary contrast values. These advantages, however, should be balanced against the increased complexity and cost of an aberration-corrected instrument. It is also important to take into consideration the information that is desired from each particular experiment.

In this chapter, we begin by providing an introduction to the basics of spherical aberration-corrected imaging in the TEM. Very few liquid cell experiments have been carried out in aberration-corrected electron microscopes at the time of writing. We therefore present representative examples of the application of spherical aberration correction in both TEM and STEM to studies of more conventional (primarily inorganic) samples. When possible, we highlight specific aspects of the designs and outcomes of these experiments that are likely to be relevant for future liquid cell studies.

After considering spherical aberration correction alone, we introduce combined chromatic and spherical aberration correction in the TEM. This is currently only available on a handful of instruments but promises to improve spatial resolution further, when compared with the use of spherical aberration correction alone. The improvements are especially clear when studying beam-sensitive samples at lower microscope accelerating voltages, examining thicker samples and acquiring atomic-resolution energy-filtered TEM (EFTEM) images using wide energy-selecting windows and large objective aperture sizes. Chromatic aberration correction also promises to further improve the precision with which the positions of features of interest in the sample can be measured and to allow atomic spatial resolution imaging when using wider objective lens pole-piece gaps.

21.2 Spherical Aberration Correction in the TEM

High resolution TEM (HRTEM) involves the acquisition of images with a spatial resolution that is sufficient to separate single atomic columns. However, the interpretation of such images is not straightforward, as the recorded intensity is rarely a direct representation of the structure in the sample. Instead, an HRTEM image can be regarded as an interference pattern that is affected by both the interaction of the incident electrons with the sample and the transfer function of the microscope.

21.2.1 Spherical Aberration and the Contrast Transfer Function

The interaction of an incident electron wave with a TEM sample can be calculated by solving the relativistically corrected Schrödinger equation for the electron wavefunction $\Psi(\boldsymbol{r})$ in the crystal potential. In the phase object approximation, the atoms in a thin sample are described by a projected electrostatic potential that is constant in the direction of the incident electron beam. After passing through a sample of thickness t, the electron wavefunction can be written in the form:

$$\Psi(\boldsymbol{r}) \approx \exp[i\phi(\boldsymbol{r},t)] = \exp[i\sigma V_{\mathrm{P}}(\boldsymbol{r})t], \tag{21.1}$$

where $\boldsymbol{r}$ is a two-dimensional vector in the plane of the specimen, ϕ is the phase of the electron wave, σ is an interaction constant that depends on the microscope voltage (kV), and V_{P} is the projected electrostatic potential. In the weak phase object approximation, it is further assumed that the change in phase of the electron wave is small after passing through a very thin sample, resulting in the expression:

$$\Psi(\boldsymbol{r}) \approx 1 + i\phi(\boldsymbol{r},t) = 1 + i\sigma V_P(\boldsymbol{r})t. \tag{21.2}$$

The effect of the microscope lenses on the recorded image intensity is described by modifying the exit plane wavefunction $\Psi(\boldsymbol{g})$ (now expressed in reciprocal space) using a phase factor $\exp[-i\chi]$ to give:

$$\Psi_i(\boldsymbol{g}) = \Psi(\boldsymbol{g})\exp[-i\chi(\boldsymbol{g})], \tag{21.3}$$

where $g = \omega/\lambda$, ω is the scattering angle, and λ is the electron wavelength. Considering only the lowest order rotationally symmetric aberrations of a round imaging lens, the aberration function takes the form:

$$\chi(\boldsymbol{g}) = 2\pi\left(\tfrac{1}{4}C_{\mathrm{S}}\lambda^3 g^4 + \tfrac{1}{2}f\lambda g^2\right). \tag{21.4}$$

In Equation (21.4), f is the defocus and C_S is the spherical aberration coefficient of the objective lens. C_S is illustrated schematically in Figure 21.1 and describes the deviation of rays that travel through the outer part of the lens compared to near-axis rays. Spherical aberration cannot be avoided for a round electromagnetic lens [1].

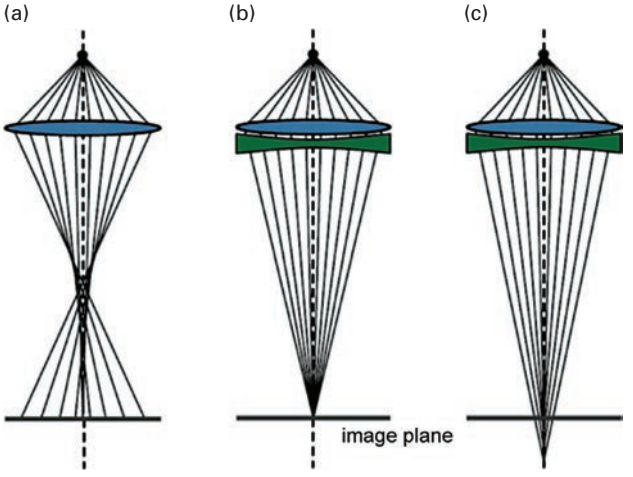

Figure 21.1. Schematic illustration of (a) positive spherical aberration, (b) no spherical aberration, and (c) negative spherical aberration.

For a very thin sample, the weak phase object approximation results in the following expression for the linear image intensity:

$$I_{\mathrm{L}}(g \neq 0) \approx 2\sigma V(g) t \sin \chi(g), \tag{21.5}$$

from which it is apparent that optimum contrast is obtained when the coherent contrast transfer function (CTF) $\sin\chi = \pm 1$, i.e. when $\chi(\boldsymbol{g})$ is an odd multiple of $\pi/2$ for all values of $\boldsymbol{g}$. However, as $\sin\chi$ is in general a function that oscillates strongly with g, atomic columns that are arranged with spacing $d = 1/g$ are imaged as white dots only for selected spatial frequencies for which the CTF is close to 1. At spatial frequencies for which the CTF is close to -1, they are imaged as black dots, while they may be invisible if the spatial frequency corresponding to their spacing coincides with a zero in the CTF.

In order to approach ideal phase contrast transfer behavior, a defocus can be chosen that balances the g^2 and g^4 terms in the aberration function χ, allowing for a relatively broad frequency band to be transferred with a CTF close to -1. This defocus setting,

$$f_{\mathrm{S}} \approx -\sqrt{\tfrac{4}{3} C_{\mathrm{S}} \lambda}, \tag{21.6}$$

is known as Scherzer defocus [2]. The point resolution $d_S = 1/g_S$ is defined by the first zero crossing of the CTF at Scherzer defocus and is given by the expression:

$$g_{\mathrm{S}} \approx \left(\tfrac{3}{16} C_{\mathrm{S}} \lambda^3\right)^{-\frac{1}{4}}. \tag{21.7}$$

Typical values of point resolution for (non-aberration-corrected) commercially available medium accelerating voltage (200–400 kV) electron microscopes are in the range 0.24–0.17 nm.

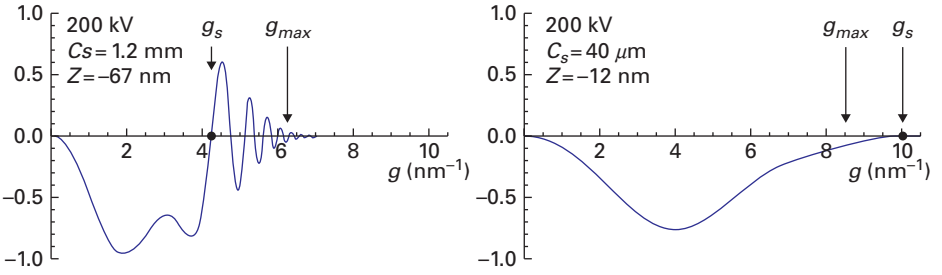

Figure 21.2. Partially coherent contrast transfer functions at Scherzer defocus calculated for a CM20 FEG TEM operated at 200 kV for (left) C_S = 1.2 mm, and (right) C_S = 0.04 mm. Z is the defocus and g_S and g_{max} are defined in the text.

The limited coherence of the electron source and electronic instabilities of the microscope have the additional effect of multiplying the coherent CTF by envelope functions, which result in a cutoff of the contrast transfer at high spatial frequencies. The spatial frequency at which the partially coherent CTF falls below a threshold defines the information limit g_{max} of the microscope, which is usually the spatial frequency at which the combined dampening envelope function drops by $1/e^2$. However, for an uncorrected field emission gun (FEG) TEM, the information limit g_{max} can be higher than the spatial frequency g_S corresponding to the point resolution, leading to strong oscillations in the partially coherent CTF and a decrease in the interpretability of images.

Figure 21.2 shows examples of the function $\sin \chi$ for a 200 kV TEM for two different values of the spherical aberration coefficient C_S. In an uncorrected electron microscope, at higher spatial frequencies the CTF oscillates rapidly up to the information limit. If C_S is reduced in a microscope that is equipped with a hardware spherical aberration corrector, then a broad transfer band extends up to the information limit of 0.125 nm, improving the point resolution significantly.

21.2.2 Delocalization Due to Spherical Aberration

As well as affecting interpretability, the oscillations of the transfer function also lead to the delocalization of information [3, 4], i.e. to the lateral displacement of high resolution image detail by a distance that depends on spatial frequency, defocus and C_S. For a homogeneous crystal with uniform thickness and translational symmetry, delocalization effects are not readily apparent. However, a discontinuity, such as an edge, locally destroys the symmetry.

Figure 21.3 shows that lattice fringes can be displaced significantly with respect to the true position of a particle. Delocalization effects are minimized in one image, despite the fact that C_S is not zero, because a single spatial frequency dominates the contrast. When a general sample is imaged in an uncorrected TEM, the effects of delocalization can usually only be minimized for a single spatial frequency at each defocus value.

If a hardware aberration corrector is not available, there is another method to overcome the effect of the strongly oscillating part of the CTF between the point

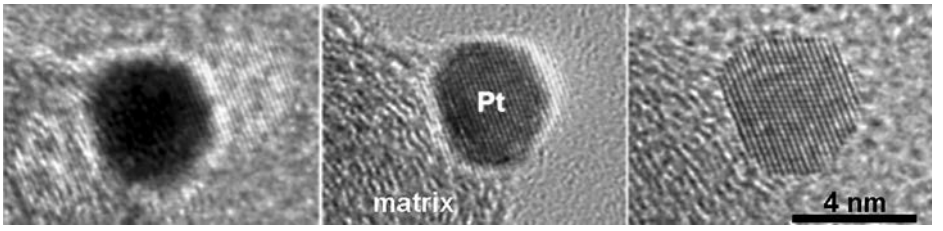

Figure 21.3. High resolution TEM images of a 5 nm Pt particle supported on graphitic C and imaged out of focus, recorded at 200 kV using a TEM that has a spherical aberration coefficient of 0.5 mm. The defocus step between successive images is 100 nm. Adapted from Ref. 4.

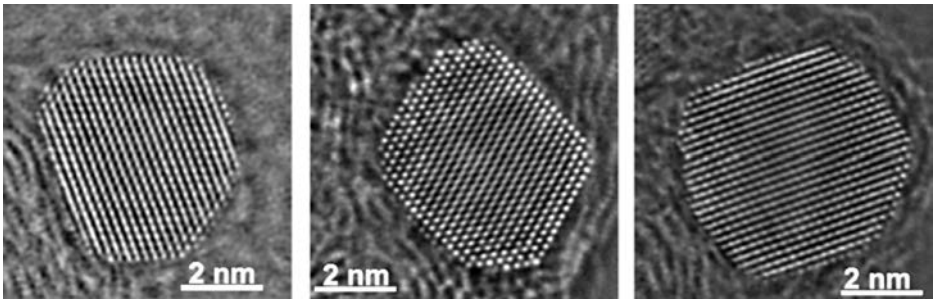

Figure 21.4. Phase images of three 5–6 nm Pt nanoparticles supported on graphitic C, obtained by applying exit wavefunction restoration to defocus series of high resolution TEM images. Adapted from Ref. 8. Reproduced with permission.

resolution and the information limit. A defocus series of typically 10–20 images is recorded from one region of the sample and software is used to numerically reconstruct the high spatial frequency components of the phase of the exit plane wavefunction [5–7]. Examples of the resulting phase images are shown in Figure 21.4.

Other similar techniques make use of multiple images recorded at different CTF settings to reconstruct the high frequency parts of the complex electron wavefunction and fill gaps in the frequency spectrum of a single image. All techniques require the sample not to change between successive images. Therefore, unless the microscope defocus can be changed rapidly and images can be acquired at a very fast frame rate, the application of exit plane wavefunction restoration to studies of materials imaged in liquid cells, in particular for real-time observations of dynamic processes, is expected to be challenging.

21.2.3 Correcting or Tuning C_S in TEM

The ability to tune the spherical aberration coefficient of the objective lens using a hardware spherical aberration corrector provides much more interpretable individual

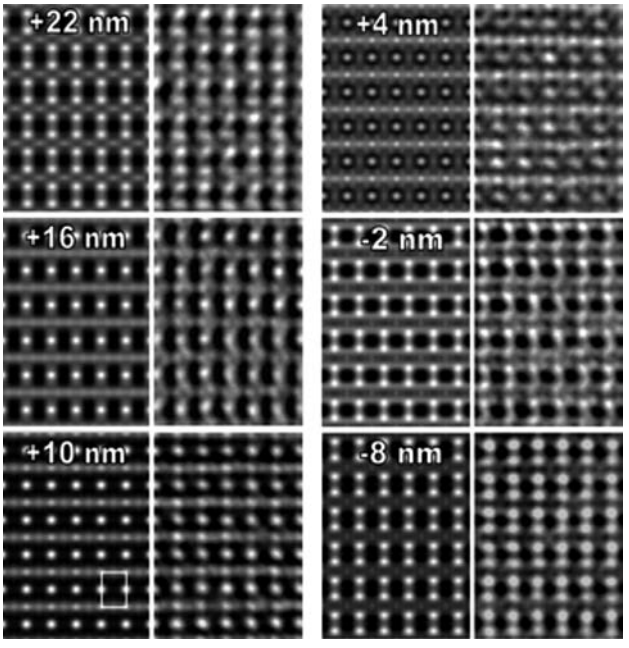

Figure 21.5. Comparison of an experimental defocus series of HRTEM images of $SrTiO_3$ oriented along [110] with simulated images. The experimental images were acquired using a C_S-corrected CM200ST FEG microscope with the value of C_S adjusted to –0.04 mm. Simulated images are shown on the left of each column, while experimental images are shown on the right. The defocus values of the simulated images are indicated. The thickness used in the simulations was 3.5 nm. Half of a $SrTiO_3$ cell projected along [110] is indicated by the white frame in the image simulated for a defocus of +10 nm. Unpublished results.

images. It is preferable to software reconstruction of the exit plane wavefunction from image series, particularly for beam-sensitive materials and for structures, such as those in liquids, that change rapidly over time.

The first truly successful demonstration of hardware spherical aberration correction in the TEM using multipole lenses was achieved in the late 1990s [9, 10]. Modern C_S-corrected transmission electron microscopes are now installed in hundreds of laboratories worldwide and are compatible with liquid cell TEM sample holders. By tuning the spherical aberration coefficient and other higher order aberrations in such instruments, it is possible to achieve optimum contrast transfer and a dramatic improvement in spatial resolution, visibility, and interpretability of individual images.

Figure 21.5 shows a comparison between an experimental defocus series of images of [110] $SrTiO_3$ recorded using a C_S-corrected Philips CM200ST FEG microscope and simulated images. A structure image predicted by simulations for a defocus of +10 nm is reproduced experimentally. Significantly, Figure 21.5 illustrates the fact that the recorded image intensity still depends sensitively on defocus (as well as on other aberrations). Comparisons of experimental images with computer simulations of image contrast are therefore usually still required for quantitative interpretation of C_S-corrected images.

The ability to tune the spherical aberration coefficient of the objective lens of a TEM using hardware provides a powerful method for recording interpretable images directly. In particular, the choice of a small negative value for C_S has been shown to result in strong contrast from columns of light atoms, which then appear bright [11]. In this so-called "negative C_S imaging" (NCSI) mode, paraxial rays that have travelled through the objective lens come to a focus ahead of outer rays. Columns of light atoms, such as O columns located adjacent to columns of heavy atoms in $Pb(Zr_{0.2}Ti_{0.8})O_3$, can then be resolved with improved contrast [12]. The ability to balance different symmetrical round aberrations in this way can be used to improve the precision of measurements of elemental composition and atom positions [13]. For a thin sample, the strong image contrast that is provided by the NCSI technique is highly sensitive to the scattering density accumulated along each atomic column. As a result, when applied in combination with image simulations, it is a valuable technique for measuring local variations in the occupancy of columns of atoms that have low nuclear charge, such as O in perovskites, as well as their positions with sub-5-pm precision [14]. A further major advantage of the NCSI technique for *in situ* experiments is its dose efficiency, since the reduced point spread and delocalization result in an optimal signal-to-noise ratio.

The significant improvement that hardware *C*s correction provides in the ability to interpret recorded HRTEM image intensities quantitatively is illustrated in Figure 21.6, which shows a recent example of the experimental application of C_S-corrected imaging to recover the three-dimensional morphology and thickness of part of an MgO crystal with atomic precision from a single image recorded under NCSI conditions [15].

In the study illustrated in Figure 21.6, precise measurements of the imaging parameters of the microscope, in combination with prior knowledge of the crystal structure of the material, allowed quantitative comparisons of the recorded image intensity with computer simulations to be performed on an absolute scale. Three-dimensional information can be recovered from just one image because electron scattering is intrinsically a three-dimensional process. A statistical confidence check was used to establish the uniqueness of the best-fitting number of atoms in each column and its position along the optical axis of the microscope relative to neighboring atomic columns, thereby allowing the surface morphology of the crystal to be determined. In future studies, it may be possible to use a similar single-image approach to follow dynamic changes in the three-dimensional morphologies of individual nanoparticles in the presence of external stimuli such as high temperature or the presence of a reactive environment in the TEM.

21.2.4 Higher-Order Aberrations and Lifetime of the Corrected State

When applying hardware spherical aberration correction, precise control and correction of residual higher-order aberrations is essential to take full advantage of the improved spatial resolution for quantitative measurements. The complete range of coherent wave aberrations can be represented by a series expansion expressed as a function of either scattering angle or reciprocal distance. Sub-angstrom resolution imaging requires

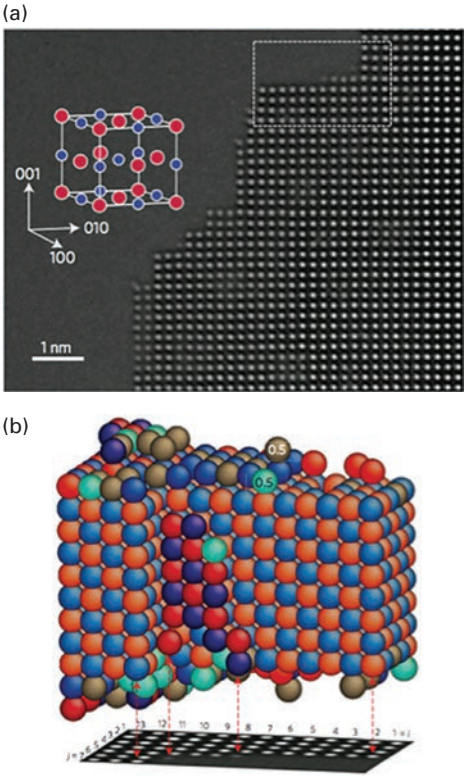

Figure 21.6. (a) C_S-corrected high resolution TEM image of an MgO crystal taken along the [001] direction under NCSI conditions. Side terraces are visible at the boundary between vacuum (left) and crystal (right). A perspective view of an MgO unit cell is shown on the left. (b) Atomically resolved view of the best-fitting three-dimensional atomic arrangement of Mg and O atoms in the region indicated in (a), based on a quantitative comparison between experimental and simulated image intensity across the region of interest. Red spheres indicate fully occupied Mg sites and blue spheres fully occupied O sites. In the surface layers, brown spheres indicate formally half-occupied Mg sites, while cyan spheres indicate formally half-occupied O sites. One possible explanation for the presence of formally half-occupied sites is the movement of surface atoms during acquisition of the image. Reproduced from Ref. 15 with permission.

both a knowledge of all significant wave aberrations up to sixth order in g and the stability of these aberrations over the time needed to acquire one or more images [16].

The decomposition of a typical aberration function into its components is illustrated in Figure 21.7, while Figure 21.8 shows an example of the time stability of the objective lens defocus measured for two different electron microscopes. After optimal alignment of a microscope, the typical lifetime of an optical state that preserves image detail up to the information limit is in most cases no longer than a few minutes [17].

The lifetime of the optical state of a microscope is, to a large extent, influenced by the thermal and environmental stability of the power supplies and the microscope lenses.

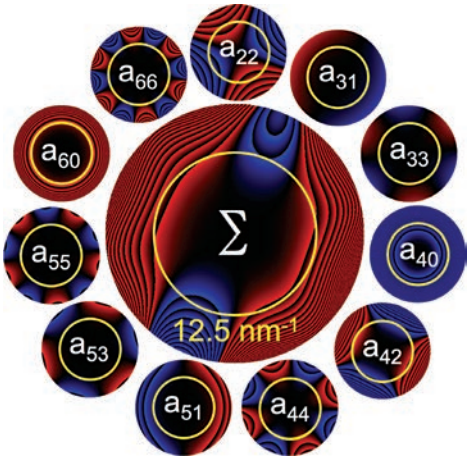

Figure 21.7. Representative aberration function (center) and its decomposition into series terms. The first index of each coefficient describes the power in g, while the second index describes the rotational symmetry. Positive values of the aberration function are depicted in red, negative values in blue. Sawtooth jumps occur at intervals of $\pi/4$. The yellow circle marks a value of $g = 12.5$ nm^{-1}, corresponding to a spatial resolution of 0.08 nm. Aberration-free imaging is achieved when the modulus of the total aberration function does not exceed $\pi/4$ within the circle that defines the resolution limit.

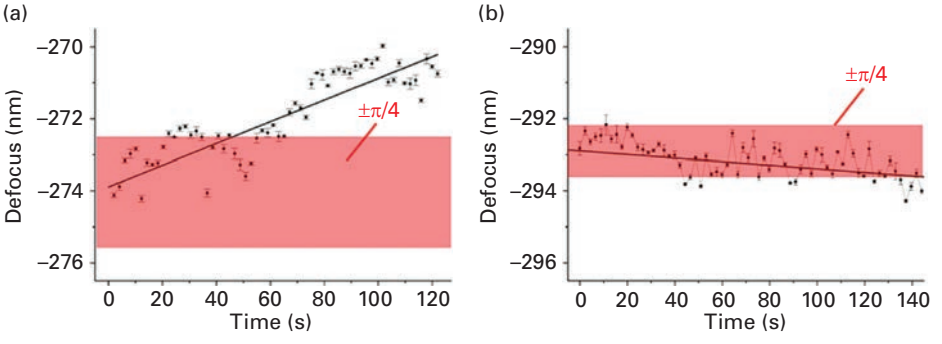

Figure 21.8. Measured time variation of the objective lens defocus over a period of approximately 2 minutes for (a) a 200 kV Philips CM200 TEM with a resolution of 0.12 nm and (b) a 300 kV FEI Titan TEM with a resolution of 0.08 nm. Both thermally induced long-term drift and short-term fluctuations caused by instabilities of the accelerating voltage and the objective lens current are observed. Unpublished data.

It can be optimized but not eliminated with today's electron optical lens designs. Therefore, continuous aberration control will also be required in future. The current state of the art is a lifetime of a few minutes at the information limit and 10–20 minutes at 1 Å resolution. For liquid cell experiments, the lifetime is likely to be much longer, since the attainable resolution, which is limited by the depth of field and multiple scattering in the sample, is worse than the optical resolution of the instrument, and since the lifetime scales approximately quadratically with resolution.

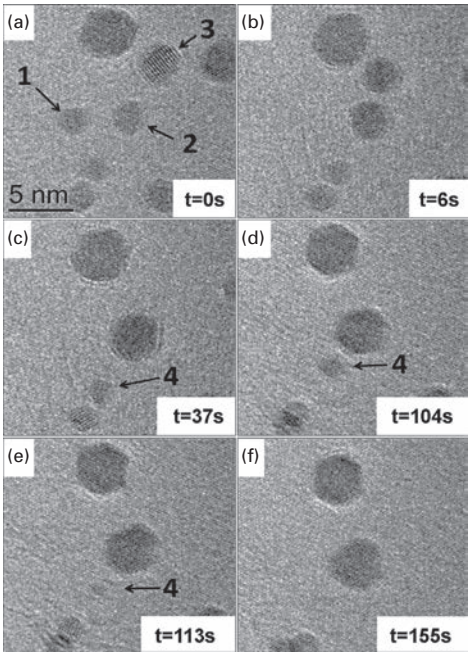

Figure 21.9. Frames taken from a sequence of HRTEM images of the sintering of a Au nanoparticle catalyst supported on BN and imaged in 130 Pa of H_2 at 410 °C at the indicated times in an environmental TEM. The images were recorded at 300 kV with the spherical aberration coefficient of the objective lens set to below 5 μm. The numbers refer to particles that undergo different sintering mechanisms. Between (a) and (b), particles 1 and 2 coalesce. Between (b) and (c), particle 3 coalesces. In contrast, particle 4 becomes smaller between (c) and (f), consistent with Ostwald ripening. Adapted from Ref. 18. Reproduced with permission.

The significant benefit of using C_S-corrected imaging to study dynamic processes in materials in real time is illustrated in Figure 21.9, in the form of a time sequence of images recorded during a gas phase sintering experiment [18]. Two primary sintering mechanisms have been proposed in such reactions, one based on the migration of particles over the support and coalescence when they are in close proximity, and the other based on Ostwald ripening, which involves mass transport from smaller to larger particles by the diffusion of atoms or molecular species. Figure 21.9 shows that both mechanisms can take place in closely adjacent regions of the same sample examined under the same conditions. Discerning such mechanistic details at the nanoparticle surfaces would have been much more difficult in an uncorrected electron microscope. Similar considerations are expected to apply to processes in liquids, such as the oriented attachment and growth experiments described in Chapters 9 and 15.

These examples serve to illustrate the significant benefit of spherical aberration correction of the TEM objective lens for atomic-resolution liquid cell studies, for which the acquisition of multiple images to improve spatial resolution or signal to noise is

difficult even when using fast electron detectors. The spatial resolution of an image of a sample in liquid can be affected by a number of factors, including scattering from both the liquid and the enclosing membranes. Nevertheless, spherical aberration correction provides significant benefits for atomic-resolution imaging, not only in terms of spatial resolution but also as a result of reduced delocalization and improved visibility and interpretability of the recorded contrast. The fact that this information can be obtained from individual recorded images, rather than using an approach such as focal series restoration and subsequent numerical processing, is especially important for real-time studies of surface and interface structures that are changing during observation. Conversely, the disadvantage of hardware spherical aberration correction when compared to focal series restoration is that the full complex electron wavefunction is not recovered and so no post-processing is possible to refocus images that occur at different depths in the liquid.

21.3 Spherical Aberration Correction in STEM

When a scanned image of a sample is recorded in a STEM using either an on-axis bright field detector or a high angle annular dark field detector, the spatial resolution is related primarily to the diameter of the focused electron probe, which is in turn determined by parameters that include the diameter of the condenser aperture and the aberrations of the condenser lens system of the microscope. Correction of the spherical aberration of the condenser lenses is therefore crucial to obtain the highest spatial resolution.

An important advantage of the HAADF image formation process is that it can be regarded as incoherent if the inner semi-angle of the detector is much larger (typically at least 100 mrad) than the semi-angle of the condenser aperture that defines the convergence angle of the illumination (typically ~20 mrad). For a sufficiently thin sample, in which the effects of beam broadening and dynamic diffraction are negligible, the recorded intensity is approximately the convolution of the square of the probe function with the square of the sample transmission function. To a good approximation, it is then proportional to the atomic number raised to the power 1.7.

A further advantage of HAADF imaging is that electron energy loss spectroscopy can be performed simultaneously, permitting the local measurement of both low (valence) energy losses (i.e. plasmon excitations, inter- and intraband transitions) and higher energy losses that are associated with inner shell ionization of atoms within the material. As the total signal in an ionization edge is proportional to the number of excited atoms, EELS can be used for quantification of the local chemical composition, typically after subtraction of the background in the spectrum acquired at each probe position using a power law expression of the form:

$$I(\Delta E, A, r) = A\,\Delta E^{-r}, \tag{21.8}$$

where ΔE is the energy loss and A and r are fitting parameters [19].

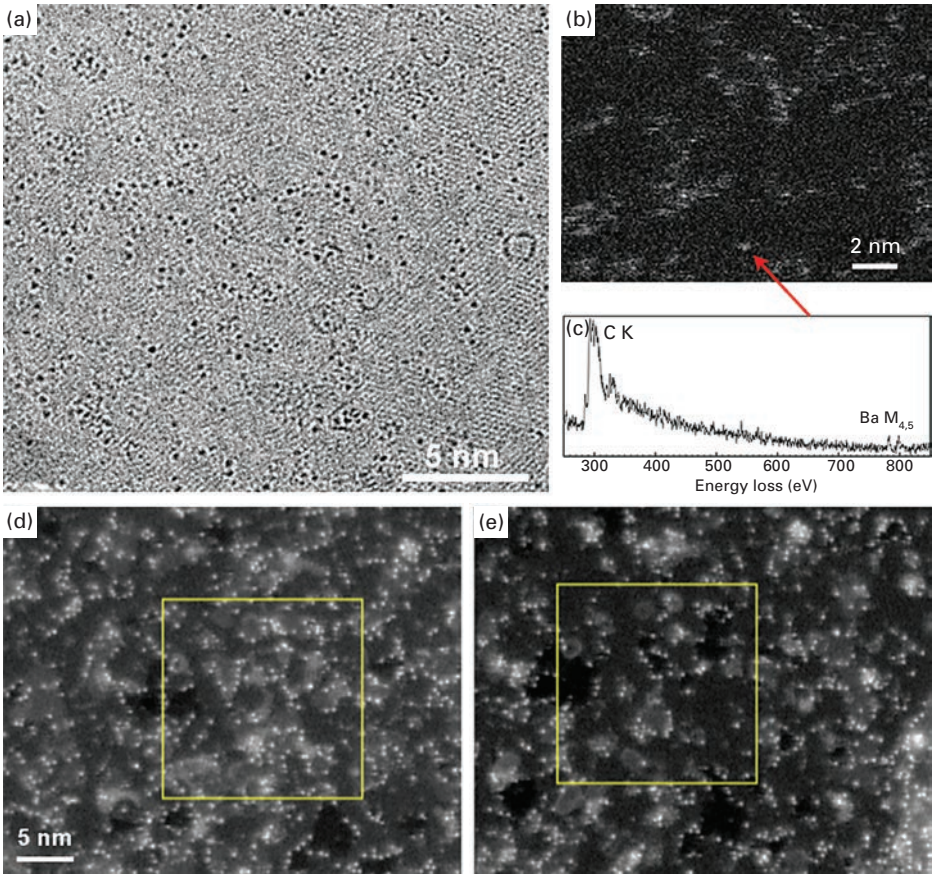

Figure 21.10. (a) High resolution TEM image of Ba-doped graphene oxide. (b) HAADF image and (c) corresponding EELS signal recorded from the indicated area during the acquisition of a spectrum image from the entire field of view. (d) and (e) HAADF images recorded before and after acquiring a spectrum image from the indicated area, showing strong bright contrast from individual Ba atoms, but also the effects of beam-induced damage both within and also to a lesser extent outside the scanned area. Adapted from Ref. 20. Reproduced with permission.

In order to illustrate the care that is required when applying aberration-corrected STEM HAADF imaging and EELS to a beam-sensitive material, as would be expected in a liquid cell experiment, Figure 21.10 shows a comparison of high resolution TEM and STEM images recorded from graphene oxide, a form of graphene whose surface is modified by the addition of functional groups [20]. This material is both sensitive to damage by the primary electron beam and highly prone to contamination during STEM imaging. As the functional groups show little contrast in HRTEM and STEM images, they were doped with Ba in order to reveal their positions. This sample required examination at low accelerating voltage (80 kV) to minimize beam damage and at elevated temperature (800 °C) to minimize contamination during imaging. Figure 21.10a shows an HRTEM image of the Ba-doped graphene oxide

sample recorded at 80 kV in a C_S/C_C-corrected TEM. In this image, the individual black dots are thought to correspond to Ba atoms, whereas in HAADF images (Figures 21.10d and e) they are imaged as bright dots with high contrast. Unfortunately, for such a sample it was found that C_S/C_C-corrected EFTEM could not be used to form elemental maps using the Ba M edge at 781eV as a result of radiation damage to the sample over the required exposure time. Instead, spectrum images acquired using EELS (i.e. background-subtracted elemental maps formed from spectra acquired point-by-point as the electron beam was scanned across the specimen) were used to identify individual Ba atoms (Figure 21.10c). A significant advantage of spectrum imaging is that the recorded signal can be correlated directly with the HAADF image intensity (Figure 21.10b). However, Figures 21.10d and e illustrate the fact that the sample is still damaged and drifts during the acquisition of each image (over ~10 mins) and that great care is required both with experimental design for studies of electron beam sensitive materials using STEM imaging and spectroscopy and with subsequent image interpretation.

21.4 Chromatic Aberration Correction in the TEM

Chromatic aberration (C_C) correction is only available on a small number of instruments worldwide at the time of writing. It is generally pursued because of the improvement in resolution limit that it provides. However, for liquid cell microscopy additional benefits of C_C correction become important. These include atomic resolution analytical EFTEM, the opportunity for more space in the sample area for *in situ* experiments, high contrast at low voltages for unstained biological materials and high resolution field-free Lorentz microscopy. In this section we discuss the opportunities that C_C correction can provide in the context of liquid cell TEM.

21.4.1 Image Resolution

In Section 21.2 we showed that the instrumental resolution of a TEM improves appreciably as a result of coherent aberration correction. C_S correction improves the spatial resolution of an uncorrected microscope from ~100 λ to ~40 λ. In order to improve the information limit further, it is also important to minimize incoherent disturbances that affect image resolution. C_C correction promises to provide a further improvement in spatial resolution to better than ~20 λ and is especially effective at lower accelerating voltages [21–24].

The primary characteristic of a C_C-corrected TEM is that the defocus f of an image remains almost constant when the electron energy varies, either due to the energy spread of the electron gun or due to the inelastic scattering of electrons within the sample. The axial chromatic change in defocus Δf associated with an energy change ΔE is given by the expression:

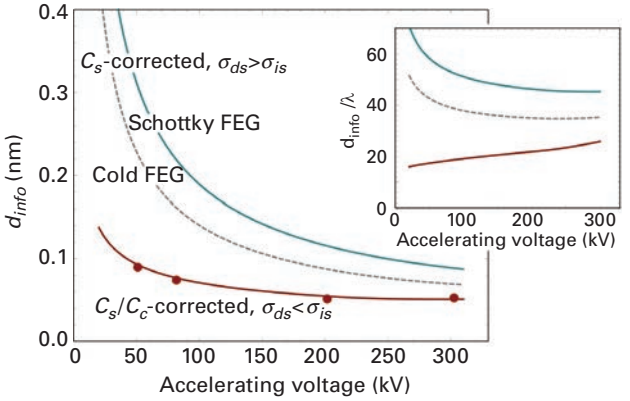

Figure 21.11. Information limit of a C_S-corrected TEM and a C_S/C_C-corrected TEM equipped with a Rose-Haider achroplanator, plotted as a function of kV. The defocus spread σ_{ds} resulting from the energy spread of the electron source determines the information limit of the C_S-corrected instrument. The cold field emitter has a better resolution than a Schottky field emitter because of a smaller energy spread. In the C_S/C_C-corrected case, the image spread σ_{is} originating from fluctuating lateral image shifts damps the high frequency transfer more strongly than the residual defocus spread due to lens instabilities. The solid curve is based on best parameter estimates between 80 kV and 300 kV and was extrapolated to lower voltages by using a linear scaling of σ_{is} with wavelength. Solid circles represent the experimental information limit measured on the PICO instrument in Jülich. The inset shows the information limit in units of wavelength. Unpublished results.

$$\Delta f(\Delta E) = C_C \frac{\Delta E}{E_0}, \tag{21.9}$$

where C_C is the chromatic aberration coefficient of the objective lens and E_0 is the energy of the primary electron beam. The greatest benefit of C_C correction is at low accelerating voltages of a few tens of kV, at which the relative energy spread is much greater than at higher kV; C_C correction is a prerequisite for atomic resolution imaging at low kV. C_C correction is most important for atomic resolution studies of materials for which low kV provides a reduction in beam-induced damage. It is potentially of great interest for liquid cell experiments, especially for studies of thick liquid layers in which inelastic scattering would normally contribute significantly to blurring of image detail.

Figure 21.11 compares, as a function of kV, the information limit of a representative C_S-corrected TEM with that of the C_S/C_C-corrected PICO TEM in Jülich, which is equipped with a Rose-Haider quadrupole-octupole achroplanator [25–27]. After the chromatic focus spread associated with the energy spread of the electron gun has been reduced in an intermediate voltage electron microscope equipped with a C_C corrector, the most significant remaining influence on instrumental resolution is associated with parasitic noise-related factors that give rise to rapid time-dependent image displacements [28]. While mechanical instabilities, lens instabilities, and time-varying stray fields may contribute to the image spread, a more fundamental limitation is magnetic field noise from thermally driven currents in the conductive parts of the instrument that cause stochastic beam deflections [29].

Within the framework of validity of linear contrast transfer theory, the influence of defocus spread and image spread on the information limit can be described in terms of a spectral damping envelope that drops by $1/e^2$ at

$$\frac{1}{d_{\mathrm{info}}} = \frac{\sigma_{\mathrm{is}}}{\lambda\sigma_{\mathrm{ds}}}\sqrt{2\left[\sqrt{1+\left(\frac{\lambda\sigma_{\mathrm{ds}}}{\pi\sigma_{\mathrm{is}}^2}\right)^2}-1\right]}, \tag{21.10}$$

where d_{info} is the information limit, σ_{ds} is the root-mean-square defocus spread, and σ_{is} is the root-mean-square image spread [24]. C_{C} correction reduces the defocus spread of the PICO TEM in Jülich by more than a factor of 10, leaving image spread as the most significant contribution to the information limit. Resolutions of 50 pm at 200 kV and 90 pm at 50 kV have been achieved after reduction of defocus spread, with a remaining major limitation due to image spread.

21.4.2 Energy-Filtered TEM

In addition to the improved information limit and contrast transfer for fine image detail described above, C_{C} correction improves resolution when images contain a significant contribution from inelastic scattering over a large energy range. This occurs in energy-filtered TEM [23, 30, 31] or because of substantial inelastic scattering through thicker objects such as liquid cells [32].

EFTEM is described in detail in Chapter 20. When acquiring energy-filtered images, C_{C} correction allows large energy windows and large objective aperture sizes to be used without compromising spatial resolution significantly. The immediate advantage of a large energy window is that imaging is more dose efficient when substantial inelastic scattering is present. C_{C} correction is therefore expected to be highly beneficial for unstained biological samples, for tilt-series tomography when the projected sample thickness at high tilt angles exceeds the inelastic mean free path, and for liquid cell experiments in which the window material and thick liquid layer cause inelastic scattering. Furthermore, the improved signal-to-noise ratio facilitates the recording of EFTEM chemical maps on the atomic scale. In each of these examples, the energy-selecting window can be extended to tens of eV in width without compromising spatial resolution.

Figure 21.12 shows the instrumental resolution for EFTEM for both a C_{S}-corrected microscope and a $C_{\mathrm{S}}/C_{\mathrm{C}}$-corrected microscope plotted as a function of collection semi-angle. In the C_{S}-corrected microscope, the instrumental resolution is limited by chromatic aberration and the diffraction limit, or, at large collection angles, by residual aberrations. Inelastically scattered electrons that fill the collection angle β homogeneously cause a chromatic broadening of

$$r_{\mathrm{C}} = C_{\mathrm{C}}\frac{\Delta E}{E_0}\beta, \tag{21.11}$$

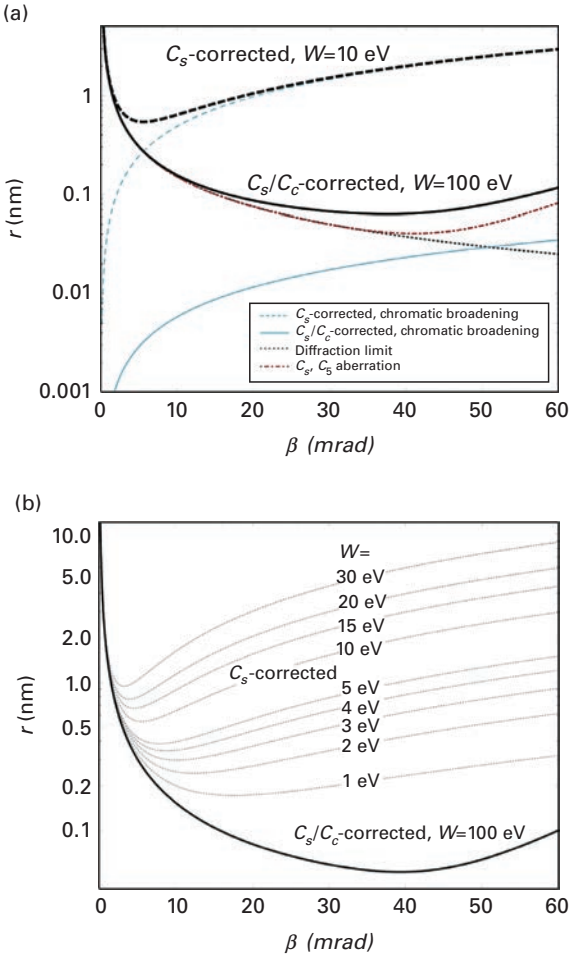

Figure 21.12. (a) EFTEM spatial resolution r plotted as a function of collection semi-angle β for a C_S-corrected instrument and a C_S/C_C-corrected TEM with field emission gun at 200 kV. The thick dashed line shows the total resolution of the C_S-corrected microscope for an energy-selecting slit width of 10 eV, whereas the thick solid line shows the total resolution of the C_S/C_C-corrected microscope for an energy-selecting slit width of 100 eV. The thin blue lines show the contribution of chromatic broadening, the grey dotted line the diffraction limit, and the red dot-dashed line the residual delocalization due to spherical aberration. In the example shown, a non-zero C_S is used to balance a higher-order spherical aberration C_5 of −4 mm for optimum phase contrast, with the reciprocal information limit β/λ. The total resolution is the sum of the residual delocalization and the chromatic broadening. (b) Total resolution plotted as a function of the width of the energy-selecting slit β. Unpublished results.

which limits the EFTEM spatial resolution in the C_S-corrected microscope to worse than a few angstroms even when the energy-selecting slit width and collection semi-angle are small. C_C correction reduces r_C by more than two orders of magnitude and provides sub-angstrom resolution when using the largest slit width and largest collection angle, as required to achieve a good signal-to-noise ratio when examining thick

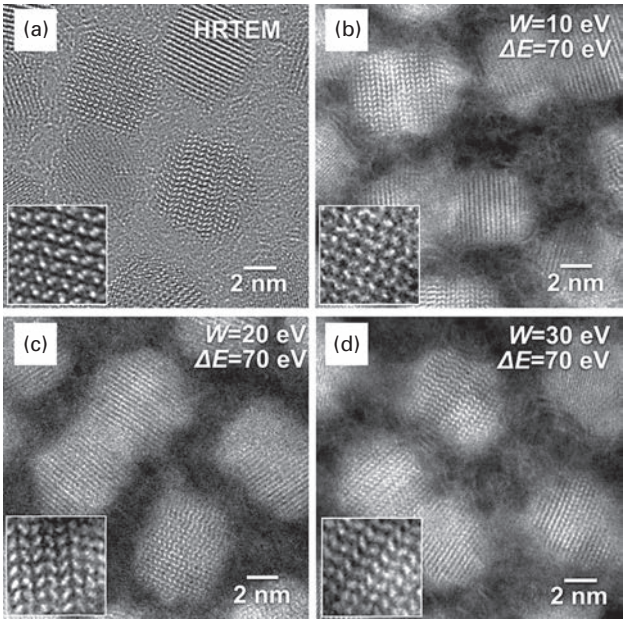

Figure 21.13. (a) High resolution and (b–d) EFTEM images of CdSe nanoparticles on a C support recorded at 80 kV in the C_S/C_C-corrected PICO instrument in Jülich. The EFTEM images were acquired using energy-selecting slit widths of 10, 20, and 30 eV with an exposure time of 20 s at an energy loss of 70 eV. They include contributions from plasmon losses and the Se M_{45} core loss. No objective aperture was used. Unpublished results.

materials or for high resolution EFTEM images, especially when the maximum tolerable dose is limited (Chapter 8).

Figure 21.13 shows that the spatial resolution in EFTEM images of CdSe nanoparticles is barely affected by the choice of energy-selecting slit width in a C_S/C_C-corrected instrument. The Cd–Se dumbbells with a spacing of 0.157 nm are resolved in each EFTEM image. It should, however, be noted that the preservation of elastic contrast can dominate atomic-resolution detail in such images, resulting in the need for comparisons with quantum mechanical image simulations for unambiguous interpretation [30, 31].

21.4.3 Thick Samples

When examining a thick sample in a C_S-corrected microscope using energy-filtered bright field TEM, the spatial resolution and depth of focus are usually optimized by reducing the chromatic broadening. This involves selecting an optimal objective aperture size, centering a narrow energy-selecting slit on the most probable energy loss that the primary electrons have suffered in the sample, and then refocusing the image to the defocus that corresponds to this most probable energy loss [33]. Figure 21.14 shows an example as applied to whole mount macrophage cells [32]. In contrast, in a C_S/C_C-corrected microscope, all electron energies and angles are in focus.

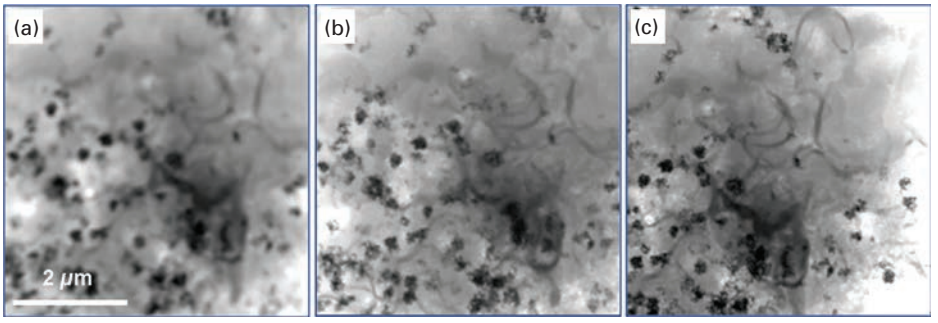

Figure 21.14. Bright field TEM images of a thick sample of a whole mount macrophage cell. (a) Energy-filtered C_S-corrected only. (b) C_C/C_S-corrected. (c) As in (a), but refocused to the most probable energy loss; (b) provides similar resolution to (c) but without excluding electrons from image formation and without the need to adjust the focus to a certain energy loss. Adapted in part from Ref. 32. Reproduced with permission.

Since inelastically scattered electrons typically lose energy without changing their direction significantly, we expect that C_C correction will allow a much larger fraction of incident electrons to be used to record high spatial resolution images of thick samples, compared to C_S correction and energy filtering alone. A further important advantage of C_C correction is that regions of the sample that have different thicknesses can all be imaged at an optimal defocus without the need to refocus to the most probable energy loss in the same field of view [32].

When a thick sample is imaged in TEM or STEM, plural elastic scattering, chromatic broadening, and defocus broadening all contribute to the loss of resolution [34]. As described in Chapter 8, in STEM, beam broadening by elastic scattering dominates and results in a distinct top–bottom effect, where objects at the top of the sample are resolved with the resolution of the unbroadened probe and those at the bottom with the resolution of the broadened probe [35–37]. In TEM, the chromatic error blurs the image detail of objects at any depth in the sample, in combination with multiple elastic scattering and the defocus error. The chromatic error is of minor importance in a C_S/C_C-corrected microscope, unlike in a conventional or C_S-corrected microscope. For the sample shown in Figure 21.14, the resolution was measured to vary between 2.5 nm and 4.5 nm between nanoparticles located at the bottom and the top of the sample, respectively, in a region of the sample of thickness 2.09 μm [32].

On the basis of reciprocity, the resolution loss due to beam divergence in STEM [38] is equivalent to depth of field and hence the effect of defocus in a C_S/C_C-corrected TEM. As chromatic broadening is no longer the limiting factor for the resolution in a C_S/C_C-corrected TEM image of a thick sample, a wide energy range of inelastically scattered electrons can be exploited. C_C correction therefore promises to be particularly beneficial for dose-optimized studies of beam-sensitive materials in liquid cells, especially when using lower accelerating voltages to attain higher contrast.

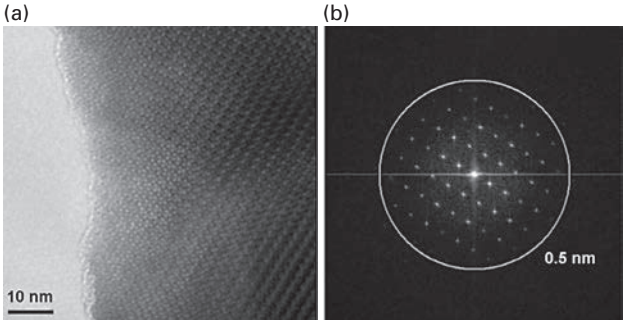

Figure 21.15. (a) C_C/C_S-corrected image of $Cs_{0.5}[Nb_{2.5}W_{2.5}O_{14}]$ [001] acquired at 300 kV in Lorentz mode with the objective lens turned off. (b) Fourier transform revealing 0.5 nm image detail. Unpublished results.

21.4.4 Wide Polepiece Gaps and Magnetic-Field-Free Imaging

A final important benefit of C_C correction results from the fact that combined C_S/C_C correction can be used to improve image resolution when using either a wide objective lens polepiece gap or a Lorentz lens. C_C correction of the Lorentz lens of a TEM allows ferromagnetic materials to be imaged with the conventional TEM objective lens switched off, i.e. in magnetic-field-free conditions, with a spatial resolution of better than 0.5 nm. Figure 21.15 shows a C_S/C_C-corrected Lorentz TEM image of $Cs_{0.5}[Nb_{2.5}W_{2.5}O_{14}]$ [001] acquired at 300 kV using the Titan PICO microscope in Jülich operated in Lorentz mode (with the objective lens turned off). The image contains 0.5 nm detail, suggesting that it may be possible to image magnetic fields in selected materials with close to atomic spatial resolution, as well as to acquire atomic-resolution images of ferromagnetic materials in liquids in magnetic-field-free conditions. For microscopes that have wide polepiece gaps, C_C correction promises to retain atomic spatial resolution while providing additional space for sophisticated holders, detectors, and other components around the sample.

21.5 Conclusions

In this chapter, we have discussed the benefits of C_S correction in TEM and STEM for liquid cell studies. These benefits include improved spatial resolution, visibility, and interpretability of images, as well as reduced delocalization of image contrast and smaller depth of field. We then described the potential benefits of combined C_S/C_C correction of the objective lens of the microscope. These benefits include an improvement in spatial resolution compared to the use of C_S correction alone, especially at low accelerating voltages, as well as the ability to study thick materials, to acquire atomic-resolution EFTEM images using large energy-selecting windows, and to improve spatial resolution in wide-polepiece-gap microscopes or microscopes that do not have an objective lens, such as those used for studies of magnetic materials.

C_S correction has been used in very few liquid cell experiments at the time of writing. However, its potential benefits are clear, especially in combination with the use of direct electron detectors and imaging energy filters. The future use of combined C_S/C_C correction also promises to allow new categories of experiments, involving thicker samples and the use of lower accelerating voltages for the examination of beam-sensitive materials at high spatial resolution.

Acknowledgements

We are grateful to Martina Luysberg, Juri Barthel, Andreas Thust, Knut Urban, Shaobo Mi, Chris Boothroyd, András Kovács, Joachim Mayer, Les Allen, Ben Forbes, Jörg Jinschek, Niels de Jonge, Jean-Pierre Baudoin, Lionel Cervera Gontard, Dogan Ozkaya, Thomas Hansen, and Maya Bar Sadan for ongoing discussions and contributions to this work.

References

1. O. Scherzer, Über einige Fehler von Elektronenlinsen. *Z. Phys*., **101** (1936), 593–603.
2. O. Scherzer, The theoretical resolution limit of the electron microscope. *J. Appl. Phys*., **20** (1949), 20–29.
3. W. Coene and A. J. Jansen, Image delocalisation and high resolution tranmission electron microscopic imaging with a field emission gun. *Scanning Microsc. Suppl*., **6** (1992), 379–403.
4. L. Cervera Gontard, R. E. Dunin-Borkowski, M. J. Hÿtch and D. Ozkaya, Delocalisation in images of Pt nanoparticles. *J. Phys. Conf. Ser*., **26** (2006), 292–295.
5. W. M. J. Coene, A. Thust, M. Op de Beeck and D. van Dyck, Maximum-likelihood method for focus-variation image reconstruction in high resolution transmission electron microscopy. *Ultramicroscopy*, **64** (1996), 109–135.
6. A. Thust, W. M. J. Coene, M. Op de Beeck and D. van Dyck, Focal-series reconstruction in HRTEM: simulation studies on nonperiodic objects. *Ultramicroscopy*, **64** (1996), 211–230.
7. C. Kisielowski, C. J. D. Hetherington, Y. C. Wang *et al*., Imaging columns of the light elements carbon, nitrogen and oxygen with sub angstrom resolution. *Ultramicroscopy*, **89** (2001), 243–263.
8. L. Cervera Gontard, L.-Y. Chang, C. J. D. Hetherington *et al.*, Aberration-corrected imaging of active sites on industrial catalyst nanoparticles. *Angew. Chem*., **46** (2007), 3683–3685.
9. M. Haider, H. Rose, S. Uhlemann *et al.*, A spherical-aberration-corrected 200 kV transmission electron microscope. *Ultramicroscopy*, **75** (1998), 53–60.
10. M. Lentzen, B. Jahnen, C. L. Jia *et al.*, High-resolution imaging with an aberration-corrected transmission electron microscope. *Ultramicroscopy*, **92** (2002), 233–242.
11. C. L. Jia, M. Lentzen and K. Urban, Atomic-resolution imaging of oxygen in perovskite ceramics. *Science*, **299** (2003), 870–873.
12. C. L. Jia, S. B. Mi, K. Urban *et al.*, Atomic-scale study of electric dipoles near charged and uncharged domain walls in ferroelectric films. *Nat. Mater*., **7** (2008), 57–61.

13. C. L. Jia, L. Houben, A. Thust and J. Barthel, On the benefit of the negative-spherical-aberration imaging technique for quantitative HRTEM. *Ultramicroscopy*, **110** (2010), 500–505.
14. C. L. Jia, J. Barthel, F. Gunkel *et al*., Atomic-scale measurement of structure and chemistry of a single-unit-cell layer of $LaAlO_3$ embedded in $SrTiO_3$. *Microsc. Microanal*., **19** (2013), 310–318.
15. C. L. Jia, S.-B. Mi, J. Barthel *et al.*, Determination of the 3D shape of a nanoscale crystal with atomic resolution from a single image. *Nat. Mater*., **13** (2014), 1044–1049.
16. J. Barthel and A. Thust, Aberration measurement in HRTEM: implementation and diagnostic use of numerical procedures for the highly precise recognition of diffractogram patterns. *Ultramicroscopy*, **111** (2010), 27–46.
17. J. Barthel and A. Thust, On the optical stability of high-resolution transmission electron microscopes. *Ultramicroscopy*, **134** (2013), 6–17.
18. T. W. Hansen, J. B. Wagner and R. E. Dunin-Borkowski, Aberration corrected and monochromated environmental transmission electron microscopy: challenges and prospects for materials science. *Mater. Sci. Technol*., **26** (2010), 1338–1344.
19. R. F. Egerton, *Electron Energy-Loss Spectroscopy in the Electron Microscope* (New York: Springer, 2011).
20. C. B. Boothroyd, M. S. Moreno, M. Duchamp *et al.*, Atomic resolution imaging and spectroscopy of barium atoms and functional groups on graphene oxide. *Ultramicroscopy*, **145** (2014), 66–73.
21. J. Zach, Chromatic correction: a revolution in electron microscopy? *Phil. Trans. R. Soc. A*, **367** (2009), 3699–3707.
22. H. Rose, Future trends in aberration corrected electron microscopy. *Phil. Trans. R. Soc. A*, **367** (2009), 3809–3823.
23. B. Kabius, P. Hartel, M. Haider *et al.*, First application of C_C-corrected imaging for high-resolution and energy-filtered TEM. *J. Electron Microsc*., **58** (2009), 147–155.
24. R. Leary and R. Brydson, Chromatic aberration correction: the next step in electron microscopy. *Adv. Imagi. Electron Phys*., **165** (2011), 73–130.
25. M. Haider, P. Hartel, H. Müller, S. Uhlemann and J. Zach, Information transfer in a TEM corrected for spherical and chromatic aberration. *Microsc. Microanal*., **16** (2010), 393–408.
26. H. Rose, Outline of an ultracorrector compensating for all primary chromatic and geometrical aberrations of charged-particle lenses. *Nucl. Instrum. Methods Phys. Res. A*, **519** (2004), 12–27.
27. H. Rose, Prospects for aberration-free electron microscopy. *Ultramicroscopy*, **103** (2005), 1–6.
28. M. Haider, H. Müller, S. Uhlemann *et al.*, Prerequisites for a Cc/Cs-corrected ultrahigh-resolution TEM. *Ultramicroscopy*, **108** (2008), 167–178.
29. S. Uhlemann, H. Müller, P. Hartel, J. Zach and M. Haider, Thermal magnetic field noise limits resolution in transmission electron microscopy. *Phys. Rev. Lett*., **111** (2013), 046101.
30. K. W. Urban, J. Mayer, J. R. Jinschek *et al.*, Achromatic elemental mapping beyond the nanoscale in the transmission electron microscope. *Phys. Rev. Lett*., **110** (2013), 185507.
31. B. D. Forbes, L. Houben, J. Mayer, R. E. Dunin-Borkowski and L. J. Allen, Elemental mapping in achromatic atomic-resolution energy-filtered transmission electron microscopy. *Ultramicroscopy*, **147** (2014), 98–105.

32. J. P. Baudoin, J. R. Jinschek, C. B. Boothroyd, R. E. Dunin-Borkowski and N. de Jonge, Chromatic aberration-corrected tilt series transmission electron microscopy of nanoparticles in a whole mount macrophage cell. *Microsc. Microanal*., **19** (2013), 814–821.
33. L. Reimer and M. Ross-Messemer, Top–bottom effect in energy-selecting TEM. *Ultramicroscopy*, **21** (1987), 385–388.
34. L. Reimer and P. Gentsch, Superposition of chromatic error and beam broadening in TEM of thick carbon and organic specimens. *Ultramicroscopy*, **1** (1975), 1–5.
35. P. Gentsch, H. Gilde and L. Reimer, Measurement of the top–bottom effect in scanning transmission electron microscopy of thick amorphous specimens. *J. Microsc*., **100** (1974), 81–92.
36. A. A. Sousa, M. F. Hohmann-Marriott, G. Zhang and R. D. Leapman, Monte Carlo electron-trajectory simulations in bright-field and dark-field STEM: implications for tomography of thick biological sections. *Ultramicroscopy*, **109** (2009), 213–221.
37. H. Demers, R. Ramachandra, D. Drouin and N. de Jonge, The probe profile and lateral resolution of scanning transmission electron microscopy of thick specimens. *Microsc. Microanal*., **18** (2012), 582–590.
38. J. K. Hyun, P. Ercius and D. A. Muller, Beam spreading and spatial resolution in thick organic specimens. *Ultramicroscopy*, **109** (2008), 1–7.